Plasmon resonances of GZO core-Ag shell nanosphere, nanorod, and nanodisk for biosensing and biomedical applications in near-infrared biological window I and II

6 authors, including:

Samar Moustafa
Assiut University
29 PUBLICATIONS   220 CITATIONS

SEE PROFILE

Jamal Q.M. Almarashi
Taibah University
33 PUBLICATIONS   561 CITATIONS

SEE PROFILE

Mohamed Rashad Ahmed
University of Tabuk
155 PUBLICATIONS   4,007 CITATIONS

SEE PROFILE

Hesham Fares
Assiut University
64 PUBLICATIONS   277 CITATIONS

SEE PROFILE

Check for updates

Plasmon resonances of GZO core–Ag shell nanospheres, nanorods, and nanodisks for biosensing and biomedical applications in near-infrared biological windows I and II†

Samar Moustafa,[ab] Jamal Q. M. Almarashi,[a] Mohamed K. Zayed,[ac] Mohamed Almokhtar,[b] Mohamed Rashad[d] and Hesham Fares [ID] *[ab]

There is currently a great deal of interest in realizing localized surface plasmon resonances (LSPRs) in two distinct windows in the near-infrared (NIR) spectrum for *in vivo* biosensing and medical applications, the biological window (BW) I and II (BW I, 700–900 nm; BW II, 1000–1700 nm). This study aims to demonstrate that LSPRs of Ga-doped ZnO (GZO) core–silver (Ag) shell structures exhibit promising features for biological applications in the NIR BW I and II. Here, we study three different shapes for nanoshells: the core–shell nanosphere, nanorod, and nanodisk. In the calculation of the optical response of these nanoshells, an effective medium approach is first used to reduce the dielectric function of a nanoshell to that of an equivalent homogenous NP with an effective dielectric function. Then, the LSPR spectra of nanoshells are calculated using the modified long-wavelength approximation (MLWA), which corrects the polarizability of the equivalent NP as obtained by Gans theory. Through numerical investigations, we examine the impacts of the core and shell sizes of the proposed nanoshells as well as the medium refractive index on the position and line width of the plasmon resonance peaks. It is shown that the plasmon resonances of the three proposed nanoshells exhibit astonishing resonance tunability in the NIR region by varying their geometrical parameters. Specifically, the improved spectrum characteristics and tunability of its plasmon resonances make the GZO–Ag nanosphere a more viable platform for NIR applications than the spherical metal colloid. Furthermore, we demonstrate that the sensitivity and figure of merit (FOM) of the plasmon resonances may be significantly increased by using GZO–Ag nanorods and nanodisks in place of GZO–Ag nanospheres. It is found that the optical properties of the transverse plasmon resonance of the GZO–Ag nanodisk are superior to all plasmon resonances produced by the GZO–Ag nanorods and GZO–Ag nanospheres in terms of sensitivity and FOM. The FOM of the transverse plasmon mode of the GZO–Ag nanodisk is almost two orders of magnitude higher than that of the longitudinal and transverse plasmon modes of the GZO–Ag nanorod in BW I and BW II. And it is 1.5 and 2 times higher than the plasmon resonance FOM of GZO–Ag nanospheres in BW I and BW II, respectively.

1. Introduction

The localized surface plasmon resonance (LSPR), a collective oscillation of electrons in metallic nanostructures induced by incident electromagnetic (EM) waves, has always been the cornerstone of *in vivo* optical applications. The LSPR phenomenon has demonstrated its impressive uses in bioimaging,[1] biomedicine,[2] and treatment of various diseases.[3] LSPR-based biosensors have been widely used in many real-time and label-free detection applications.[4] LSPR biosensors offer numerous advantages, including low cost, greater surface to volume ratio, simultaneous detection of several targets, and real-time molecular binding monitoring.[5,6] Moreover, LSPR induces a high-intensity localized electric field in the vicinity of plasmonic nanoparticles (NPs) with a shorter decay length, which improves the sensitivity of NPs toward the change in the refractive index of the surroundings. The absorption of light

[a] Physics Department, College of Science, Taibah University, P. O. Box 30002, Medina, Saudi Arabia. E-mail: hfhassan@taibahu.edu.sa

[b] Department of Physics, Faculty of Science, Assiut University, Assiut 71516, Egypt

[c] Physics Department, Faculty of Science, Beni-Suef University, Beni-Suef 6111, Egypt

[d] Physics Department, Faculty of Science, University of Tabuk, Tabuk 71491, Saudi Arabia

This journal is © the Owner Societies 2024

Phys. Chem. Chem. Phys., 2024, **26**, 17817–17829 | 17817

by living tissues is very low in the near-infrared (NIR) biological window I (BW I) of 700–900 nm and biological window II (BW II) of 1000–1700 nm, increasing the depth of light penetration in the living body. A vast number of efforts have been conducted by researchers to realize LSPRs in BW I and BW II for improving the state-of-the-art of biosensing and biomedical technology.[7–10] For most biomedical applications including detection, imaging, and treatment, LSPR with high sensitivity and a narrow bandwidth is highly in demand.

The LSPR wavelengths of plasmonic NPs are influenced by their size, structure, shape, and material as well as the dielectric properties of the surrounding medium. In the case of conventional gold (Au)/silver (Ag) nanospheres, the increase in the particle size allows the LSPR wavelength to be tuned from the ultraviolet (UV) to the NIR. However, larger nanospheres (roughly >100 nm in diameter) exhibit LSPR with a broad asymmetric line shape due to retardation effects, making the induced NIR LSPR undesirable for medical applications. High LSPR sensitivity, strong field enhancement, and excellent resonance tunability can be achieved by using nanostructures with various shapes, particularly nanotriangles,[11] nanorods,[12,13] and nanodisks.[14] Au nanorods with different aspect ratios have been exploited for multiplexed sensing by monitoring the distinctive LSPR peak shift induced by the attachment of three different molecules to their surfaces.[5] In another study, Au nanoprisms have been utilized to identify and quantify the microRNAs (*i.e.*, a prognostic cancer biomarker) in the blood of cancer patients.[15] NIR plasmon resonances with high sensitivity can be achieved using core–shell NPs with a thinner metal shell. The plasmon resonance wavelength's tunability can be feasibly attained by changing the shell thickness, in addition to the material and geometry of NPs.[16–19] The configuration of hollow metal nanoshells receives remarkable interest for sensing applications.[20,21] Anisotropic shapes of the nanoshell structure, such as nanorod and nanodisk, allow additional degrees of freedom to enhance the optical features of the induced LSPR.[22]

The performance of plasmonic devices operating in the NIR regime, including the BW I and BW II regime, is severely limited by the large optical losses in noble metals. Recently, non-stoichiometric transparent conducting oxides (TCOs), such as zinc oxide (ZnO), tin oxide (SnO$_2$), and cadmium oxide (CdO), have emerged as potential substitute materials to replace noble metals in low-loss plasmonic applications.[23] Among all TCO materials, ZnO is an attractive material for microscale and nanoscale devices because of its considerable thermal and environmental stability, excellent durability, non-toxicity, low cost, and easy preparation.[24] By doping ZnO and other TCOs with foreign atoms, it is feasible to adjust their plasmon resonance wavelength from near IR to mid IR by raising the carrier density level (10^{19} cm^{-3}–10^{21} cm^{-3}).[25] Doping can significantly improve the optical, electrical, chemical, and structural properties of ZnO.[26] The enhanced photoresponse in the ZnO wide-bandgap materials is mainly due to the improved light absorption mediated by dopant atom states. Therefore, extrinsic ZnO nanostructures are widely used to enhance the performance of various ZnO-based applications

including gas sensing,[27] solar cells,[28] and photocatalysis.[29] Ga has low reactivity and strong conductivity, making it an astonishing ZnO dopant. Since the covalent bond length of Ga–O of 1.92 Å is so close to that of Zn–O $\sim$1.97 Å, Ga-doped ZnO (GZO) shows lower electrical resistivity and higher electron mobility.[30] Ga doping extends the plasmon wavelength of ZnO NPs to the NIR region up to 4 μm.[31] GZO NPs can sustain an IR plasmon finding extensive use in several applications like transparent contacts for solar cells, optoelectronic devices, nanocrystalline ink precursors for printing film, and touch screens.[32] In this study, we utilize GZO in our NP models as a good demonstrative example for TCO materials, without sacrificing the generalizability of the main findings if we replace it with other doped-TCOs, such as Al-doped zinc oxide (AZO) and tin-doped indium oxide (ITO).

In this study, the LSPRs of nanoshell configurations with a GZO–core and an Ag–shell are theoretically investigated. We examine three distinct geometries of GZO–Ag nanoshells: the core–shell nanosphere (spherical nanoshell), nanorod, and nanodisk. As mentioned above, the findings of this study will not be changed if other materials of TCOs (like AZO or ITO) and/or other noble metals (like Au) are used. In our simulations of the optical response of GZO core–Ag shell nanorods/nanodisks, an effective medium approach (EMA) is used to obtain the dielectric function of nanoshells as that of an equivalent homogenous spheroidal particle. Next, the polarizability of spheroidal particles computed using Gans theory, which is only applicable in the small particle regime, is corrected using the modified long-wavelength approximation (MLWA). In this work, it is shown that the LSPR of GZO–Ag core–shell nanostructures can be tuned over the entire UV-visible-IR region, including BW I and BW II, by varying the shell thickness and/or core size. It is shown that the use of TCO materials (like GZO) as a core material in metal nanoshells, instead of traditional lossless dielectric materials such as SiO$_2$, significantly enhances the tunability range of the plasmon resonance. For the assumed nanoshell structures, we investigate the impact of the geometrical parameters of spherical, rod-shaped, and disk-shaped nanoshells on the sensitivity and bandwidth of the LSPR. It is shown that the nanodisk nanoshell has a higher sensitivity and narrower bandwidth than the spherical and nanorod nanoshells. We also elucidate the advantageous of the studied GZO–Ag nanoshells over other traditional structures such as Ag nanospheres and nanorods.

2. Methods and materials

Fig. 1 shows the schematics of the three different shapes of GZO–Ag core–shell structures that are investigated in this research, namely spherical, prolate (rod-like), and oblate (disk-like). In Fig. 1(a), a GZO–Ag nanosphere consists of a GZO core of radius r_1 coated with an Ag shell of thickness d and is immersed in a matrix. The dielectric function of the core, shell, and matrix are ε_c, ε_s, and ε_{med}, respectively. For the purpose of comparing the investigated nanoshells, we identify

17818 | *Phys. Chem. Chem. Phys.*, 2024, **26**, 17817–17829

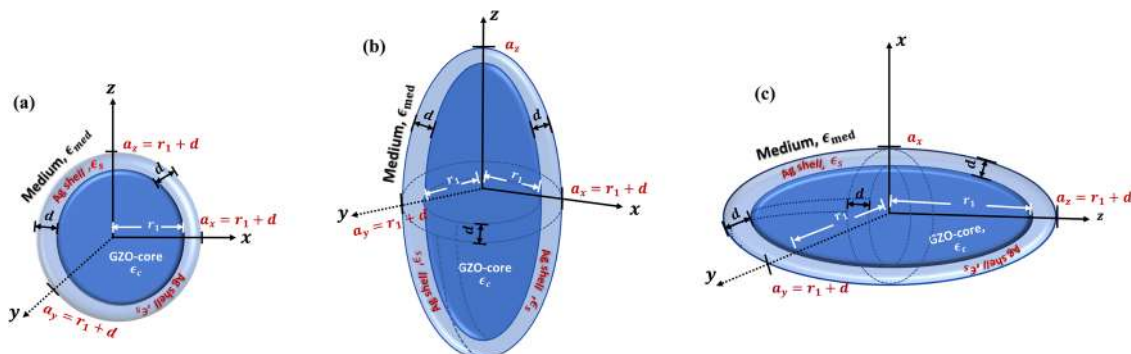This journal is © the Owner Societies 2024

Fig. 1 Schematic of GZO–Ag (a) spherical, (b) rod-shaped, and (c) disk-shaped nanoshells that have been investigated in this study.

the size of the spherical nanoshell in the x-, y-, and z-directions as a_x, a_y, and a_z, respectively. For the spherical nanoshell shown in Fig. 1(a), $a_x = a_y = a_z = r_1 + d$. A schematic of a GZO–Ag rod-shaped nanoshell is shown in Fig. 1(b), where the major axis (longitudinal direction) is along the x-direction, and the minor axes (transverse directions) are along the y- and z-directions. In the simulations, we assume the length of the nanorod is set at 100 nm ($2a_x = 100$ nm) and $a_y = a_z = r_1 + d$. Fig. 1(c) shows a schematic illustration of a GZO–Ag disk-shaped nanoshell where the minor axis (longitudinal direction) is along the z-direction, and the major axes (transverse directions) are along

computationally challenging. In order to relax the computation complexity, we use the effective medium method allowing us to obtain the effective dielectric function of the nanoshell as that of an equivalent homogenous system.[33,34] Then, the computation of the plasmonic response of a nanoshell is simplified to that of a single particle. In this work, we investigate the accuracy of three widely used EMAs in estimating the effective dielectric function of core–shell NPs, weighted average (WA),[35] Maxwell–Garnett (M–G),[36] and internal homogenization (IH)[33] approaches. In these EMAs, the effective permittivity $\varepsilon_{\mathrm{eff}}$ of a nanoshell is calculated by

$$
\left\{
\begin{array}{ll}
\varepsilon_{\mathrm{eff}} = f\varepsilon_{\mathrm{c}} + (1-f)\varepsilon_{\mathrm{s}}, & \text{(Weighted average)} \\[2mm]
\varepsilon_{\mathrm{eff}} = \varepsilon_{\mathrm{s}}\dfrac{(\varepsilon_{\mathrm{c}} + 2\varepsilon_{\mathrm{s}}) + 2f(\varepsilon_{\mathrm{c}} - \varepsilon_{\mathrm{s}})}{(\varepsilon_{\mathrm{c}} + 2\varepsilon_{\mathrm{s}}) - f(\varepsilon_{\mathrm{c}} - \varepsilon_{\mathrm{s}})}, & \text{(Maxwell} - \text{Garnett)} \\[2mm]
\varepsilon_{\mathrm{eff}} = \dfrac{1+2\chi}{1-\chi}, \chi = \dfrac{(\varepsilon_{\mathrm{s}} - 1)(\varepsilon_{\mathrm{c}} + 2\varepsilon_{\mathrm{s}}) + f(\varepsilon_{\mathrm{c}} - \varepsilon_{\mathrm{s}})(1 + 2\varepsilon_{\mathrm{s}})}{(\varepsilon_{\mathrm{s}} + 2)(\varepsilon_{\mathrm{c}} + 2\varepsilon_{\mathrm{s}}) + 2f(\varepsilon_{\mathrm{c}} - \varepsilon_{\mathrm{s}})(\varepsilon_{\mathrm{s}} - 1)}, & \text{(Internal homogenization)}
\end{array}
\right\}, \qquad (2)
$$

the y- and x-directions. Our assumptions for the simulations are that the nanodisk's length is fixed at 10 nm ($2a_z = 10$ nm) and that $a_y = a_x = r_1 + d$.

The sensitivity factor S, a commonly used metric of nanostructure sensitivity, is defined as the resonance wavelength change of the plasmon peak λ_{res} relative to the change in the refractive index unit (RIU) of the host medium n_{med},

$$
S = \frac{\mathrm{d}\lambda_{\mathrm{res}}}{\mathrm{d}n_{\mathrm{med}}}. \qquad (1)
$$

Resonance peak shifts linked to the variation in the medium refractive index become undistinguished as the LSPR spectrum widens. Therefore, the linewidth is another crucial metric for assessing the performance of LSPR sensors in biological applications. The LSPR linewidth is commonly quantified by the figure of merit (FOM) factor, defined as the ratio of the sensitivity parameter S to the full width at half maximum (FWHM) of the LSPR peak (FOM = $S/\Delta\lambda_{\mathrm{FWHM}}$). LSPR sensors must concurrently address both requirements, a high sensitivity and a sharp LSPR spectrum.

In this paper, we investigate the optical response of relatively large core–shell NPs with complex geometries, which is

where $f = (r_1^3)/(r_2^3)$ is the filling factor representing the core volume fraction. In the following section, we shall compare the accuracy of EMAs given by eqn (2) in describing the absorption spectra of the nanoshells under consideration. Next, we employ the MLWA for accounting the correction to the absorption cross section of ellipsoidal homogenous particles calculated by the Gans theory.[37] Below, we will briefly go over Gans theory and MLWA providing the fundamental equations of both approaches.

For sensing and biomedical applications, regardless of the structural model of NPs, the use of small NPs (*i.e.*, the particle size is approximately ≤ 100 nm) is highly in demand for the following main reasons: (i) the optical absorption of the small particle has a dominant effect over the scattering effect, resulting in an appreciable thermal dissipation that serves as the basis for biomedical therapeutic applications. (ii) The high sensitivity and tunability of the resonance wavelength are feasibly achieved using small particles.[12] For small particles, the optical response of NPs can be described by the quasistatic approach in which the EM phase shift is neglected inside the NP. Spheroidal particles (*e.g.*, oblate and prolate spheroids) may have sufficient volume, such that the spontaneous

This journal is © the Owner Societies 2024

Phys. Chem. Chem. Phys., 2024, **26**, 17817–17829 | 17819

emission of radiation by induced dipole (light scattering) could be appreciable in comparison to the light absorption. Also, in the spheroidal NPs case, we must take into account the depolarization of radiation across the particle surface due to the non-homogenous response of electrons along the principal axis.[38,39] In this study, although we are principally interested in the small particle regime, we use the MLWA to account for the size- and shape-corrected polarizability associated with the radiation damping and dynamic depolarization.[40,41] The MLWA permits us to evaluate the radiation damping and depolarization contribution separately, make it advantageous over numerical methods for plasmonic NPs, including the finite difference time domain (FDTD), discrete dipole approximation (DDA), and finite element method (FEM).[42] The surface scattering effect on the plasmon resonance is taken account separately in the dielectric function of the core and shell components.

Within the quasistatic dipole approximation, the induced dipole of the LSPR along the principal axis ($i = x, y, z$) $\boldsymbol{p}_i$ is given by[36]

$$\boldsymbol{p_i} = \varepsilon_{\mathrm{m}}\alpha_i \boldsymbol{E}_{\mathrm{inc},i}, \tag{3}$$

where $\boldsymbol{E}_{\mathrm{inc},i}$ and α_i are the incident EM field and the polarizability of the NP along the principal axis, respectively. In the small particle regime, α_i of the ellipsoidal particles according to Gans theory is given by

$$\alpha_i = \frac{4\pi a_x a_y a_z}{3}\frac{\varepsilon_{\mathrm{eff}} - \varepsilon_{\mathrm{m}}}{\varepsilon_{\mathrm{m}} + L_i(\varepsilon_{\mathrm{eff}} - \varepsilon_{\mathrm{m}})},$$
$$L_i = \frac{a_x a_y a_z}{2}\int_0^\infty \frac{\mathrm{d}q}{(a_i + q)f(q)}, \tag{4}$$

where L_i is the geometrical factor that satisfies $\sum_i L_i = 1$. In eqn (4), the function $f(q) = [(q + a_x{}^2)(q + a_y{}^2)(q + a_z{}^2)]^{1/2}$. For a sphere (a special ellipsoid with $a_x = a_y = a_z$), $L_x = L_y = L_z = 1/3$. Noting in eqn (4) that the core–shell structure is represented as a homogeneous particle with an effective permittivity $\varepsilon_{\mathrm{eff}}$ which is given by an EMA in eqn (2).

The prolate (rod-shaped) and the oblate (disk-shaped) spheroids have two axes of equal length. Therefore, only one of the geometrical factors is independent. In the case of the oblate spheroid for which $a_x = a_y > a_z$ (i.e., the minor axis is in the z-direction), L_i is given by[36]

$$L_x = L_y = \frac{g(e)}{2e^2}\left\{\frac{\pi}{2} - \tan^{-1}[g(e)]\right\} - \frac{g^2(e)}{2}, \quad L_z = 1 - 2L_x, \tag{5}$$

where $g(e) = [(1 - e^2)/e^2]^{1/2}$ and the eccentricity $e = 1 - (a_z{}^2/a_x{}^2)$. On the other hand, in the case of the prolate spheroid for which $a_z = a_y < a_x$ (i.e., the major axis is in the x-direction), L_i becomes

$$L_x = \frac{1 - e^2}{e^2}\left[\frac{1}{2e}\ln\left(\frac{1+e}{1-e}\right) - 1\right], \quad L_y = L_z = \frac{1 - L_x}{2}, \tag{6}$$

where $e = 1 - (a_y{}^2/a_x{}^2)$. The shape of the oblate and prolate spheroids ranges from a disk ($e = 1$) and a needle ($e = 1$) to a sphere ($e = 0$), respectively.

According to the MLWA, the size-corrected dipole moment $\boldsymbol{p}_i^{(\mathrm{MLWA})}$ is given by[43]

$$\boldsymbol{p}_i^{(\mathrm{MLWA})} = \varepsilon_{\mathrm{m}}\alpha_i^{(\mathrm{MLWA})}\boldsymbol{E}_{\mathrm{inc},i}, \quad \alpha_i^{(\mathrm{MLWA})}$$
$$= \frac{\alpha_i}{[1 - (ik^3\alpha_i/6\pi) - (k^2\alpha_i/4\pi a_i)]}, \tag{7}$$

where α_i shown in eqn (4) is obtained by Gans theory and $k = 2\pi\sqrt{\varepsilon_{\mathrm{m}}}/\lambda$ is the wavenumber of the light in the surrounding medium. The term of the radiation damping associated with a large volume of NPs scales by k^3 while the term of the radiation depolarization due to the non-homogenous response of electrons scales by k^2. For randomly oriented particles, the cross sections of absorption and scattering are obtained using the relationships

$$\sigma_{\mathrm{abs}} = k\sum_i \mathrm{Im}\left(\alpha_i^{(\mathrm{MLWA})}\right), \quad \sigma_{\mathrm{sca}} = \frac{k^4}{6\pi}\sum_i \left|\alpha_i^{(\mathrm{MLWA})}\right|^2. \tag{8}$$

Here, it is worth drawing attention to the approach developed by Schebarchov *et al.* in ref. 44, wherein accurate analytical expressions for the optical response of metallic nanoshells have been presented taking into account the radiative correction of electrostatic solutions. The MLWA, which is employed in this study to incorporate the radiative correction, correctly predicts the LSPR properties of the proposed nanoshells. However, the approach developed in ref. 44 could be a potential alternative to the MLWA.

The Drude–Lorentz oscillator model provides an accurate description of the dielectric function of the bulk TCOs.[45] In our simulations, we employ the Drude–Lorentz parameters, as published in ref. 46. These parameters accurately describe the experimental dielectric permittivity of GZO (6 wt%) within the spectral range spanning from 350 nm to 2000 nm. It is worth noting that if we use the Drude–Lorentz parameters published in other papers and describe other dielectric permittivity measurements,[47] no discernible difference to the results of this work is found. Involving the damping of the plasmons due to the electron scattering at the core surface, the dielectric function of the GZO core can be calculated using[46]

$$\varepsilon(r_{\mathrm{eff}}, \omega) = \varepsilon_\infty - \frac{\omega_{\mathrm{p}}^2}{\omega(\omega + j\Gamma_{\mathrm{mod}})} - \frac{f_1\omega_1}{\omega_1^2 - \omega^2 - j\omega\Gamma_1}. \tag{9}$$

where ε_∞ is the background permittivity, ω_{p} is the plasma frequency, f_1 is the strength of the Lorentz oscillator with center frequency ω_1 and damping Γ_1. Γ_{mod} is the corrected bulk collisional frequency taking into account the effect of size-dependent electron scatterings, being given by

$$\Gamma_{\mathrm{mod}} = \Gamma_0 + A\frac{v_{\mathrm{f}}}{r_{\mathrm{eff}}}, \tag{10}$$

where Γ_0 is the bulk collisional frequency, r_{eff} is the mean free path of free charges (*i.e.*, $r_{\mathrm{eff}} = 2r_1$ for the core and $r_{\mathrm{eff}} = d$ for the shell in eqn (11)), v_{f} is the Fermi velocity, and A is a geometric parameter. In this study, the geometric parameter A is assumed to have a value of 1.[48] The electron concentration n_{e} in the TCOs is in the range of $(\sim 10^{19}–10^{21})$ cm^{-3}[47] while the effective mass

17820 | *Phys. Chem. Chem. Phys.*, 2024, **26**, 17817–17829

This journal is © the Owner Societies 2024

of an electron m_e^* is in the range of $(0.3-0.7)m_e$. m_e^* of GZO equals $0.4m_e$ when $n_e = 10^{21}$ cm^{-3}.[49] For GZO, by using these values of m_e^* and n_e in the Fermi velocity expression $v_f = (\hbar/m_e^*)(2\pi n_e)^{1/2}$, one finds that the damping rate due to the surface scattering $(Av_f/2r_1)$ has an unimportant contribution with respect to the bulk electron scattering Γ_0 ($\Gamma_0 \sim 0.1$ eV for GZO) when $r_1 \geq 3$ nm. Therefore, the relaxation rate of electron-surface collisions can be neglected for the assumed range of the GZO core radius. In contrast, in the metallic shell region, the damping of electron-surface collisions plays a major role. The parameters of the Drude–Lorentz model shown in eqn (9) for GZO (6 wt%) as given in ref. 46 are $\varepsilon_\infty = 2.475$, $\omega_p = 1.927$ eV, $\Gamma_0 = 0.117$ eV, $f_1 = 0.866$ eV, $\omega_1 = 4.850$ eV, and $\Gamma_1 = 0.029$ eV.

Using notations similar to those in eqn (9), the Lorentz–Drude theory is also used to describe the dielectric function of the Ag shell, being given by[50]

$$\varepsilon(r_{eff}, \omega) = \varepsilon(\omega)_{exp} + \frac{\omega_p^2}{\omega^2 + j\omega\Gamma_0} - \frac{\omega_p^2}{\omega^2 + j\omega\Gamma_{mod}}. \quad (11)$$

In eqn (11), $\varepsilon(\omega)_{exp}$ is the experimental bulk dielectric function, and is calculated by[51]

$$\varepsilon(\omega)_{exp} = 1 - \frac{\Omega_p^2}{\omega^2 + j\omega\Gamma_0} + \sum_{j=1}^{N} \frac{f_j\omega_p^2}{(\omega_j^2 - \omega^2) - j\omega\Gamma_j}. \quad (12)$$

where $\Omega_p = \sqrt{f_0}\omega_p$ is a normalized plasma frequency associated with intraband transitions with oscillator strength f_0 and damping constant Γ_0. In eqn (12), the contribution of interband transitions to the dielectric constant is determined by the second term in eqn (12) where j is the number of oscillators with frequency ω_j, strength f_j, and lifetime $1/\Gamma_j$. In this work, we utilize the values provided in ref. 51 for the Lorentz–Drude parameters of Ag in eqn (11) and (12) that accurately predict the experimental measurement of the Ag dielectric function.

3. Results and discussions

The results of MLWA deviate from the exact results of Mie theory when the multipolar effects become significantly pronounced. Furthermore, EMAs may not be practical for large nanoshells, *i.e.*, when the size of the equivalent sphere is much larger than the incident wavelength.[52] Therefore, before proceeding to the numerical simulations, we must check the accuracy range of the core and shell size over which our theoretical approach is valid. For this purpose, we make various comparisons between the optical response of spherical nanoshells as obtained by Mie theory and that obtained by the MLWA. These comparisons are carried out for spherical nanoshells consisting of an Ag–shell and a GZO–core (GZO–Ag nanosphere) assuming different core and shell dimensions. Here, we assume the refractive index of the host medium $n_{med} = 1.33$. The code of multilayered Mie theory was developed by our group in MATHCAD software using the algorithm proposed by Toon and Ackerman in ref. 53. In Fig. 2(a)–(c), we plot the normalized absorption cross-section σ_{abs} *versus* the light wavelength where σ_{abs} is calculated using the Mie theory for a spherical nanoshell and using the MLWA for an equivalent spherical nanosphere whose effective dielectric function is determined by the AW, MG, and IH methods given by eqn (2). As shown by Fig. 2(a) and (b), σ_{abs} calculated using the MLWA combined with the MG (or IH) approach is almost identical to that obtained by the Mie theory. In Fig. 2(a), even when the shell thickness is quite small ($d = 2$ nm), a significant deviation is shown between σ_{abs} obtained by the Mie theory and the MLWA with the AW method. In Fig. 2(c), when $d = 8$ nm, a little deviation begins to appear between the results of the Mie theory and the MLWA with the MG (or IH) method. It is evident from Fig. 2 that the effective dielectric approaches of MG and IH are nearly identical and far better compared to the AW approach. Strictly speaking, the MLWA with the MG (or IH) method precisely predicts the absorption cross-section when $r_1 \leq 50$ nm and $d \leq 8$ nm. In fact, we are particularly interested in this range of core size and shell thickness where a significant
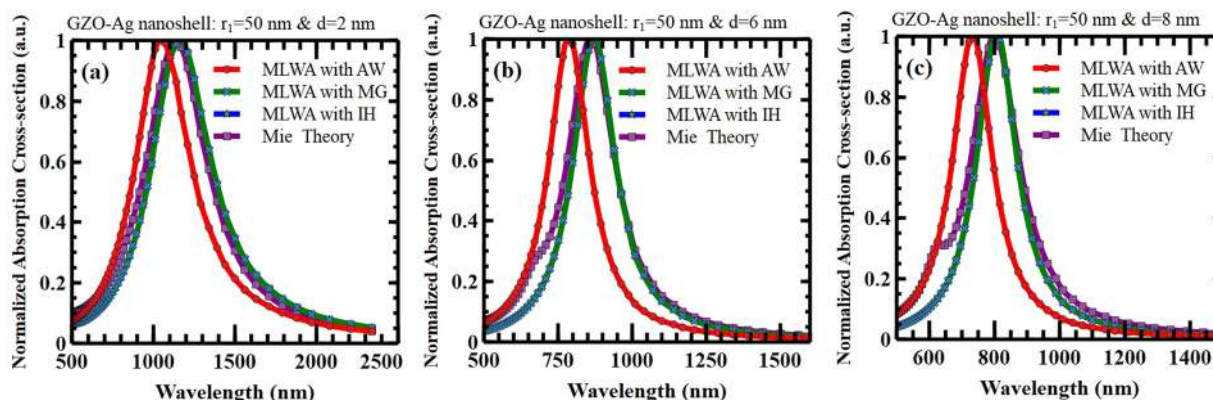

Fig. 2 Comparisons between the normalized absorption cross-section as calculated by Mie theory and by the MLWA in combination with one of three effective medium methods, weighted average (WA) or Maxwell–Garnett (M–G) or internal homogenization (IH) methods. For these comparisons, we assume a GZO–Ag spherical nanoshell when $r_1 = 50$ nm and (a) $d = 2$ nm, (b) $d = 6$ nm, and (c) $d = 8$ nm.

absorption with a narrow linewidth can be achieved for high-performance sensing and medical applications.

As revealed by eqn (2), the filling factor f is the key variable in calculating the effective dielectric function ε_{eff} of composite NPs, regardless of the NPs' shape. In addition to the filling factor, the effective medium approaches depend on the difference between the indices of refraction of the core and shell. Based on this, our procedure based on the MLWA with the MG (or IH) approach is valid for core–shell nanorods and nanodisks when their filling factor f equals (or smaller than) that of spherical nanoshells whose $r_1 \leq 50$ nm and $d \leq 8$ nm. Recalling that $f = r_1^3/r_2^3$ for spherical nanoshells and $f = r_1^2/r_2^2$ for core–shell nanorods and nanodisks, the maximum shell thickness in the rod-shaped and disk-shaped nanoshells is given by

$$d_{\max} = r_1 \left\{ \left[1 + \frac{8(\text{in nm})}{r_1} \right]^{\frac{3}{2}} - 1 \right\}. \qquad (13)$$

In the following simulations, we assume $10 < r_1 < 50$, and then $d_{\max} \leq 12.5$.

Based on the above, the MLWA can be used for calculating the extinction cross-sections of spherical nanoshells, instead of the Mie theory, in the range of $r_1 \leq 50$ nm and $d \leq 8$ nm. However, in the following, the exact Mie theory is sometimes used for calculating the absorption coefficient $Q_{\text{abs}} = \sigma_{\text{abs}}/A_s$ of spherical nanoshells, where A_s is the geometric cross section of the particle. Then, we overcome any restrictions on the core and/or shell sizes.

Our theoretical approach consists of two steps: (i) the use of the effective medium theory to obtain the dielectric function of nanoshells as that of an equivalent homogenous particle, and (ii) the use of Gans theory, corrected by the MLWA, to calculate the absorption coefficient of the equivalent particle. The effective medium methods, defined by eqn (2), are independent of the nanoshell's shape and are dependent on the volume fraction of the core f and the difference between the refractive indices of the core and shell. The second step depends on the particle size with respect to the incident wavelength in the x-, y-, and z-directions independently. By means of comparisons with the Mie theory, we determine the validity range of the core and shell sizes in our methodology for spherical nanoshells. Next, the corresponding validity range of the core and shell sizes for non-spherical nanoshells is determined by assuming the filling factor of spherical and non-spherical nanoshells is the same and considering the maximum possible dimensions of spherical nanoshells. To assure the credibility of our proposed theoretical approach for non-spherical nanoshells, we will now compare our results with theoretical and experimental results published by other authors for non-spherical shapes.

In ref. 54, the authors used the DDA method for describing the LSPR features of silica-core gold-shell nanorods. The complex refractive index of Au was assumed to be equal to that of the bulk metal. The surrounding medium was supposed to be water, with a refractive index of 1.33, while the silica core was considered to have a refractive index of 1.44 at all wavelengths. In ref. 54, four structural design cases have been studied for which $2a_x = 2a_y = 10$ nm and $2a_z = 80$ nm (*i.e.*, the symbols $2a_x$, $2a_z$, and d in Fig. 1(b) in this paper correspond to S_o, L_o, and $(L_o - L_i)/2$ in ref. 54). In Fig. S1(a) and (b) in the ESI,† we illustrate the extinction spectra of the silica–gold rod-like nanoshells as calculated by our approach assuming the same geometrical parameters as in Fig. 1 of ref. 54. In Table 1, we present comparisons between the LSPR features of nanoshells predicted by our approach and those obtained by the DDA method as reported in ref. 54. In Table 1, the first, second, and third column, respectively, show the peak wavelength λ_{res} and FWHM of the plasmon resonances as determined by Gans theory with the MLWA and Maxwell–Garnett method (*i.e.*, the method applied in this work), Gans theory with the Maxwell–Garnett method, and the DDA method as in ref. 54. In the second and third columns, we provide the deviation magnitude δ (in %) from the values of the present study. In ref. 54, the assumed the shell thicknesses are greater than the maximum thickness assumed in this study given by eqn (13), nevertheless, a very satisfactory matching between the results of our method (first column) and those of the DDA method (third column) has been noted. For longitudinal modes of the third and fourth case study, λ_{res} obtained by our method begins to diverge noticeably from that obtained by the DDA. We consider that this discrepancy is plausible where the shell thickness d in the third and fourth cases ($d = 24$ nm and 26 nm) greatly exceeds the limiting value of d proposed in our method ($d_{\max} \leq 12.5$). Also, it is noteworthy that the difference observed between the results of our approach and the DDA method may be attributed to the approximations utilized by both methods. For instance, the accuracy of our method is influenced by the filling factor along with the size and materials type of the core and shell. On the other hand, the shape errors linked to the surface dipoles of the particle could reduce the accuracy of the DDA method.[55] For longitudinal modes, comparisons presented in Table 1 indicate a larger deviation from the DDA results when applying Gans theory with the Maxwell–Garnett technique without using the MLWA (second column). Therefore, the use of MLWA for correcting the polarizability obtained by Gans theory is critical to realize the matching between our results and those of the DDA method.

In the ESI,† Fig. S2 shows excellent agreement between the peak position of the absorption bands of silica coated Au nanorods calculated using our approach and the measured ones reported in ref. 56. In the experiments reported in ref. 56, silica-coated Au nanorods were immersed in ethanol whose refractive index is approximately 1.36. Prior to coating with silica, the Au nanorods had longitudinal and transverse diameters of 52.5 nm and 15 nm, respectively (*i.e.*, using our symbols, $2a_z = 52.5$ nm and $2a_x = 2a_y = 15$ nm). After coating with silica, the shell thicknesses of silica were 10 nm, 12 nm, and 14 nm. The measured FWHMs are approximately 2.6 times larger than the FWHMs of the calculated absorption peaks in Fig. S2 (ESI†). Indeed, the measured absorption spectra are anticipated to be wider than those of a single particle due to the inhomogeneous broadenings caused by the variations in the

17822 | *Phys. Chem. Chem. Phys.*, 2024, **26**, 17817–17829

This journal is © the Owner Societies 2024

Table 1 For silica–gold rod-shaped nanoshells with different shell thicknesses, comparisons between the results obtained by our approach and those obtained using the DDA method as reported in ref. 54 are given. The first, second, and third columns, respectively, display the peak wavelength λ_{res} and FWHM of LSPRs as determined by Gans theory with MLWA and Maxwell–Garnett effective method (our applied method), Gans theory with Maxwell–Garnett method, and the DDA method as in ref. 54. In the second and third columns, the deviation magnitude δ (in %) from the values of the present study is shown

	Gans theory + MLWA + Maxwell–Garnett method • The applied method in this study	Gans theory + Maxwell–Garnett method	DDA method as reported in ref. 54
Case (1): r_1 = 24 nm and d = 16 nm,			
Trans. mode (λ_{res}, FWHM)$\approx$	(580 nm, 79 nm)	(567 nm, 86 nm) δ (in %) $\approx$ (2.2, 8.8)	(564 nm, 102 nm) δ (in %) $\approx$ (2.7, 29.1)
Long. mode (λ_{res}, FWHM)$\approx$	(905 nm, 68 nm)	(893 nm, 68 nm) δ (in %) $\approx$ (1.3, 0.0)	(935 nm, 71.7 nm) δ (in %) $\approx$ (3.3, 5.4)
Case (2): r_1 = 20 nm and d = 20 nm,			
Trans. mode (λ_{res}, FWHM)$\approx$	(550 nm, 80 nm)	(545 nm, 76 nm) δ (in %) $\approx$ (0.9, 5.0)	(534 nm, 91 nm) δ (in %) $\approx$ (2.9, 13.7)
Long. mode (λ_{res}, FWHM)$\approx$	(831 nm, 64 nm)	(821 nm, 60 nm) δ (in %) $\approx$ (1.2, 6.2)	(870 nm, 78 nm) δ (in %) $\approx$ (4.7, 21.8)
Case (3): r_1 = 16 nm and d = 24 nm,			
Trans. mode (λ_{res}, FWHM)$\approx$	(532 nm, 82 nm)	(529 nm, 80 nm) δ (in %) $\approx$ (0.5, 2.4)	(524 nm, 72 nm) δ (in %) $\approx$ (1.5, 12.2)
Long. mode (λ_{res}, FWHM)$\approx$	(781 nm, 64 nm)	(771 nm, 58 nm) δ (in %) $\approx$ (1.2, 9.3)	(840 nm, 60 nm) δ (in %) $\approx$ (7.5, 6.2)
Case (4): r_1 = 14 nm and d = 26 nm,			
Trans. mode (λ_{res}, FWHM)$\approx$	(522 nm, 90 nm)	(515 nm, 92 nm) δ (in %) $\approx$ (1.3, 2.1)	(516.6 nm, 77.5 nm) δ (in %) $\approx$ (1.0, 13.8)
Long. mode (λ_{res}, FWHM)$\approx$	(763 nm, 62 nm)	(752 nm, 58 nm) δ (in %) $\approx$ (1.4, 6.4)	(822 nm, 70 nm) δ (in %) $\approx$ (7.7, 12.9)

size and shape of NPs.[57,58] Another issue that could result in an additional broadening in the measured plasmon bandwidth is the chemical surface damping caused by imperfections at the NP-medium interface.[58,59] Also, when the particle–particle distance is small enough, the strong near-field coupling between the evanescent fields of individual particles causes variations in the absorption spectra of a single particle.[60] Let us close this section by emphasizing that the limiting range of the nanoshell geometrical parameters in our methodology needs to be re-examined if another combination of core and shell materials is

used. For different nanoshell structure models, an effective medium method rather than the Maxwell–Garnett method may be more beneficial.

Fig. 3(a) shows the absorption spectra of spherical composite NPs consisting of a GZO core of radius r_1 = 40 nm and an Ag shell with different thicknesses d = 2, 4, 8, and 16 nm. In this figure and all subsequent figures unless specified otherwise, we use n_{med} = 1.33. In Fig. 3, the absorption spectra of spherical GZO–Ag nanoshells are calculated using exact Mie theory which is valid for arbitrary core and shell sizes. Fig. 3 includes the
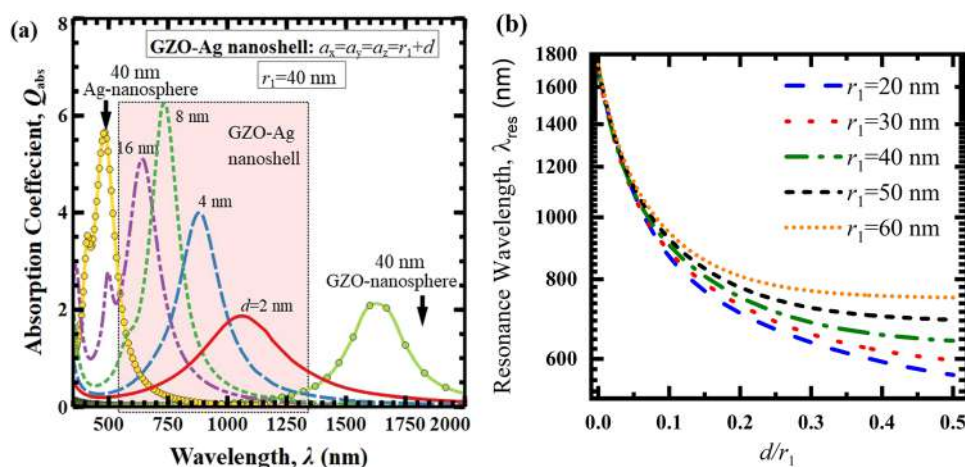

Fig. 3 (a) The absorption spectra of the GZO–Ag core–shell spherical nanoshell (GZO–Ag nanosphere) at different values of shell thickness d and constant core radius r_1 = 40 nm. Also, the absorption spectra Ag and GZO nanospheres with a fixed radius r_1 = 40 nm are shown. (b) Variation of the resonance wavelength λ_{res} of the GZO–Ag nanosphere with the ratio of the shell thickness to core radius d/r_1 at different core radiuses r_1.

This journal is © the Owner Societies 2024

Phys. Chem. Chem. Phys., 2024, **26**, 17817–17829 | **17823**

absorption spectrum of Ag and GZO nanospheres with a fixed radius $r_1 = 40$ nm. It is seen that Ag and GZO nanospheres show a plasmon resonance peak at $\lambda_{res} \sim 490$ nm and ~ 1625 nm, respectively. Reading the figure from right to left, the plasmon resonance of the GZO–Ag nanosphere blue shifts with increasing the Ag shell thickness d. This is due to the fact that when d increases, the effective dielectric constant ε_{eff} of the nanoshell approaches ε_s of Ag, and hence, the plasmon resonance of the GZO–Ag nanosphere approaches that of Ag nanosphere. Fig. 3 elucidates a highly sensitive tunability in the range of small shell thickness (*i.e.*, when d varies from 0 to 4 nm). In the thick Ag shell range (*i.e.*, when $d \geq 8$ nm), the blue-shift amount of the plasmon resonance reduces. It is also shown that a narrower plasmon linewidth is observed as the plasmon resonance blue shifts to smaller resonance wavelengths. In the NIR spectral range (for $\lambda_{res} > 700$ nm when $d < 8$ nm), the line shape of the plasmon resonance is symmetric. The symmetry property of the plasmon resonance becomes deceptive at large Ag shell thicknesses ($d > 8$ nm) where a small shoulder peak of the quadrupole plasmon mode becomes evident. Indeed, a plasmon resonance in the NIR can be achieved by increasing the size of the Ag nanosphere. But, as the size of metal nanospheres increases, the plasmon absorption is significantly degraded at the expense of an increase in the scattering process and the plasmon peak becomes asymmetric due to the quadrupole effects.[61] Therefore, the plasmon resonance characteristics of metal nanospheres (like Ag nanospheres) are significantly deteriorated in the NIR range limiting the use of metal collides in NIR applications. On the other hand, GZO–Ag nanospheres show attractive LSPR features with wide optical tunability in the NIR range of the spectrum, including BW I and BW II. Therefore, the potential use of this class of nanoshell in biological applications will be promising. In Fig. 3(b), we plot the variation in the resonance wavelength λ_{res} of the GZO–Ag nanosphere with the ratio of the shell thickness to core radius d/r_1 at different core radiuses r_1. From Fig. 3(b), it is demonstrated that the GZO–Ag nanosphere can induce a plasmon resonance peak anywhere within the visible to infrared region by changing the ratio d/r_1. Fig. 3(b) illustrates that the blue shift of the plasmon resonance of GZO–Ag nanospheres is greater as d/r_1 increases up to 0.1. As d/r_1 increases further, the amount of the blue shift of the plasmon peak decreases.

This study proposes substituting commonly used lossless dielectric materials (like Si and SiO_2[62]) as a core coated with metals in metal nanoshells with TCO materials (*e.g.*, GZO). Here, we discuss the reasoning behind the potential superiority of the GZO core over the dielectric core in metal nanoshells. In Fig. 4, we plot the absorption spectra of GZO–Ag, SiO_2–Ag, and TiO_2–Ag spherical nanoshells when the thickness of the Ag shell $d = 1, 2, 3,$ and 4 nm assuming a fixed core radius $r_1 = 40$ nm. SiO_2 and TiO_2 represent dielectric materials with low and high dielectric permittivity coefficients, respectively. The dielectric constant of SiO_2 and TiO_2 are taken to be as reported in ref. 63 and 64, respectively. As shown by Fig. 4(a)–(c), when the thickness of the Ag shell is relatively thin ($d = 1, 2,$ and 3 nm), the GZO–Ag structure exhibits LSPR in the NIR with a

narrower bandwidth and better tunability than that exhibited by SiO_2–Ag and TiO_2–Ag structures. Moreover, the magnitude of the absorption coefficient in the GZO–Ag nanosphere is greater than that of the SiO_2–Ag nanosphere when $d \leq 3$ nm. As the Ag shell thickness reaches 4 nm, the characteristics of the plasmon resonance of the GZO–Ag and SiO_2–Ag structures become nearly the same. However, whatever the shell thickness d, the spectral linewidth and tunability of LSPR in GZO–Ag and SiO_2–Ag structures are superior to those of TiO_2–Ag LSPR. Overall, it appears that the replacement of the dielectric core with the GZO core in metal nanoshells is beneficial to exhibit LSPRs in the NIR range with improved characteristics in terms of linewidth narrowing and a wider tunability range.

In Fig. (5), we merely elucidate the basic characteristics of the plasmon modes of GZO–Ag nanorods and nanodisks. To provide a more comprehensive picture in Fig. (5), we will assume that the electric field of the incident light has two components in the direction of the long and short axes of the nanorods and nanodisks. Then, the electric field can excite electron oscillations along both axes simultaneously. In Fig. 5(a) and (b), the length of the nanorod structure in the direction of major axis (x-axis in Fig. 1(b)) is assumed constant at 100 nm ($2a_x = 100$ nm). In Fig. 5(a), the Ag shell thickness d is taken to be constant at 2.5 nm and the radial length r_1 varies from 6 nm to 14 nm with a 2 nm increment step. In Fig. 5(b), in contrast, r_1 is assumed to be constant at 12 nm and d is varied from 2 nm to 8 nm with a 2 nm increment. In Fig. 5(a) and (b), two plasmon resonance peaks of GZO–Ag nanorods are exhibited: one is a longitudinal mode (LM) and the other is a transverse mode (TM) which corresponds to electron oscillations along the long and short axes of the rod, respectively. In Fig. 5(a), the radial length r_1 increases whereas the rod-like nanoshell approaches a spherical nanoshell, the TM red shifts while the LM blue shifts tending to be combined into a single peak associated with the spherical shape. In Fig. 5(b) when the radial length r_1 is fixed, the TM and LM red shift with decreasing the Ag shell thickness d, in a similar behavior to that of the plasmon mode of the spherical nanoshell in Fig. 3(a). From Fig. 5(a) and (b), it is demonstrated that by choosing appropriate parameters of GZO–Ag nanorod, TM and LM can be operated simultaneously in the first and second biological windows (*e.g.*, when $r_1 = 12$ nm and $d = 2.5$ nm in Fig. 5(a)). In Fig. 5(c), the length of the GZO–Ag nanodisk structure in the direction of the minor axis (z-axis in Fig. 1(c)) is assumed to be constant at 10 nm ($2a_z = 10$ nm). The radial length r_1 is assumed to be constant at 30 nm and the Ag thickness d takes the values of 2, 4, 6 and 10 nm. Similar to the nanorod-shaped particles, the GZO–Ag nanodisk exhibits longitudinal and transverse plasmon modes attributed to the minor and major particle sizes, respectively. Fig. 5(c) demonstrates that the longitudinal resonance is almost unnoticed in the spectra where the particle size in the direction of minor axis is relatively very small with respect to that in the direction of the major axis. As in the case of the GZO–Ag spherical and rod-shaped nanoshells, Fig. 5(c) shows that the transversal and longitudinal resonances of the GZO–Ag nanodisk red shifts as the shell thickness decreases.
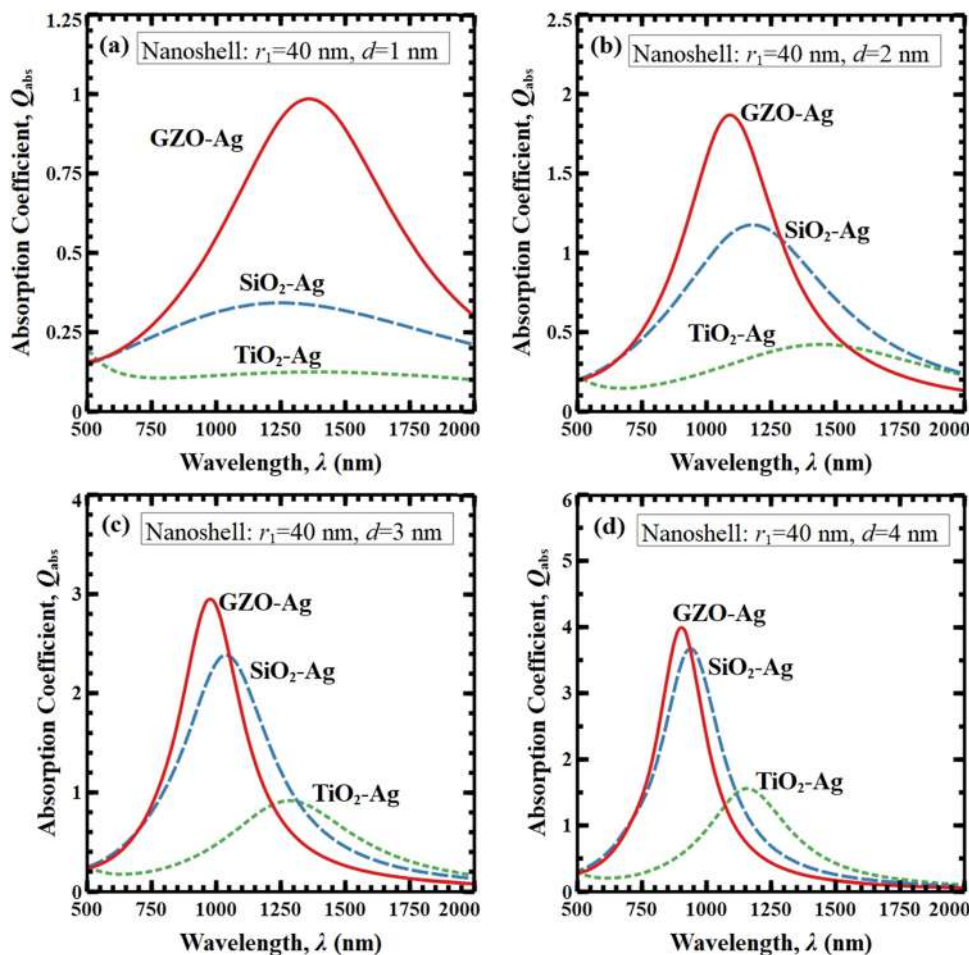
17824 | *Phys. Chem. Chem. Phys.*, 2024, **26**, 17817–17829

This journal is © the Owner Societies 2024

Fig. 4 The absorption spectra of GZO–Ag, SiO$_2$–Ag, and TiO$_2$–Ag spherical nanoshells with a core radius of r_1 = 40 nm and shell thickness d of (a) 1 nm, (b) 2 nm, (c) 3 nm, and (d) 4 nm.
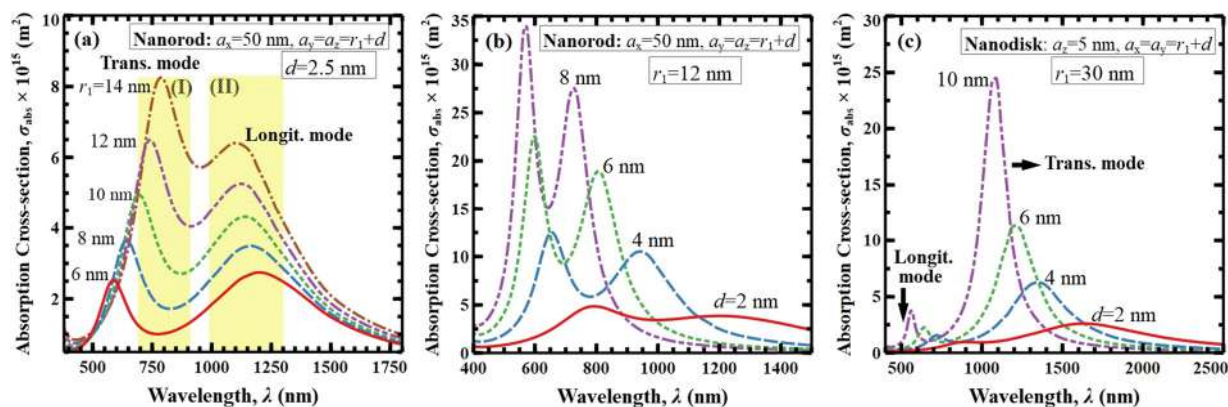

Fig. 5 The absorption spectra of the GZO–Ag nanorod with a constant length of 100 nm in the major-axis direction when (a) the Ag shell thickness d = 2.5 nm and the radial length r_1 = 6, 8, 10, and 12 nm, (b) the radial length r_1 is constant at 12 nm and the Ag shell thickness d = 2, 4, 6, and 8 nm. (c) The absorption spectrum of the GZO–Ag nanodisk with a constant length of 10 nm in the minor-axis direction when the radial length r_1 is constant at 30 nm and the Ag shell thickness d = 2, 4, 6, and 10 nm.

In Fig. 6(a) and (b), we plot the resonance wavelength λ_{res} (on the left axis) and the full width at half maximum (FWHM) (on the right axis) of plasmon resonance peaks *versus* the shell thickness d for GZO–Ag and Ag nanorods. Fig. 6(a) and (b) are dedicated for longitudinal and transversal resonances, respectively. In Fig. 6, we assume the longitudinal length of
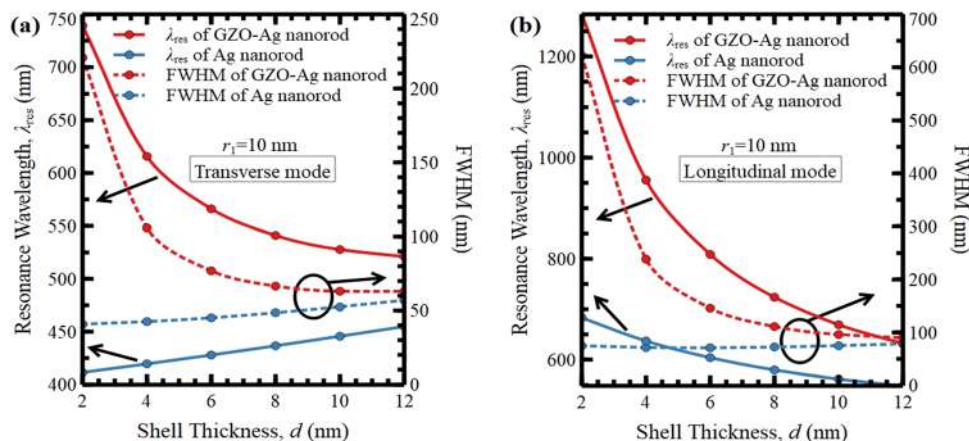
Fig. 6 For GZO–Ag and Ag nanorods, comparisons between the resonance wavelength and the full-width at half maximum (FWHM) of the (a) transverse resonance mode and (b) longitudinal resonance mode.

the GZO–Ag nanorod is 100 nm (in x-direction), the radial length r_1 = 10 nm, and the thickness of the Ag shell is variable. The longitudinal length of the Ag nanorod is also fixed at 100 nm, as in the GZO–Ag nanorod, while its transverse size (in y- and z-directions) equals the sum of $2r_1$ and d of the GZO–Ag nanorod. In Fig. 6(b), it is shown that the longitudinal resonance wavelength of the GZO–Ag nanorod can be tuned over a broad range in the visible and NIR regions, approximately from 1300 nm to 600 nm as the Ag thickness is changed from 2 nm to 12 nm. On the other hand, the resonance wavelength of the Ag nanorod is tuned over a relatively very small range, from 690 nm to 550 nm for the same range of Ag thickness. The same conclusion can be drawn from Fig. 6(a) when comparing the tuning of the transversal resonance wavelength of GZO–Ag and Ag nanorods with changing the shell thickness d. Fig. 6(a) and (b) demonstrate that the GZO–Ag nanorod significantly surpasses the traditional Ag nanorod structure in terms of tunability. In Fig. 6(a) and (b), the FWHM is widely varied in association with the wide tunning range of the resonance wavelength. However, it is worth noting that the FWHM of the longitudinal plasmon resonance is remarkably smaller than that of the transversal plasmon resonance at the same resonance wavelength. The above findings of GZO–Ag nanorods hold true for GZO–Ag nanodisks when comparing their LSPR with those of Ag nanodisks.

In Fig. 7, we compare the sensitivity factor S given by eqn (1) and FOM = S/λ_{FWHM} of the GZO–Ag spherical nanoshell, GZO–Ag nanorod, and GZO–Ag nanodisk, focusing on the spectral wavelength range of BW I and BW II when the refractive index of the medium n_{med} is varied over its range of biological tissues ($\sim$1.3–1.8).[65] Here, we select the geometrical parameters of the considered structure so that the resonance wavelength of its plasmon mode is varied along BW I or BW II as n_{med} changes from 1.3 to 1.8. Based on this, for the GZO–Ag spherical nanoshell, we assume a constant radial length r_1 = 30 nm and assume Ag shell thicknesses of d = 7 nm and d = 2 nm in Fig. 7(a and b)– and (c and d) devoted to BW I and BW II, respectively. We use a longitudinal length of GZO–Ag nanorod

of 100 nm (the x-direction in Fig. 1(b)) and that of the GZO–Ag nanodisk is 10 nm (the z-direction in Fig. 1(c)), respectively. For the GZO–Ag nanorod, we assume r_1 = 13 nm and d = 3.3 nm so that the TM and LM scan over BW I and BW II when n_{med} = 1.3–1.8, respectively. For the GZO–Ag nanodisk, as shown in Fig. 5(c), the LM is very weak since the longitudinal size of the nanodisk is relatively very small in comparison to its size in the transverse directions. Then, we are only interested in the TM in the case of disk-shaped nanoshells. Here, we assume a constant shell thickness d = 10 nm and assume r_1 = 13 nm and 30 nm in Fig. 7(a and b)– and (c and d) devoted to BW I and BW II, respectively. From Fig. 7(a)–(d), it can be seen that the sensitivity factor S and FOM of the nanodisk TM are significantly higher than those of the GZO–Ag nanosphere and GZO–Ag nanorod in BW I and BW II. As shown in Fig. 7(a) and (c), S of the GZO–Ag nanodisk TM is 390.1 nm per RIU and 668.7 nm per RIU in BW I and BW II, respectively. As shown in Fig. 7(b) and (d), the FOM of the GZO–Ag nanodisk TM is almost two orders of magnitude higher than the LM and TM of the GZO–Ag nanorod over the entire range of n_{med}. And that the FOM of the GZO–Ag nanodisk TM is 1.5 and 2 times higher than the plasmon resonance of the GZO–Ag spherical nanoshell in BW I and BW II, respectively. Comparing the S factor of GZO–Ag nanorod plasmon resonances and that of GZO–Ag spherical nanoshells in BW I and BW II shown in Fig. 7(a) and (c), respectively, it is found that the S of the GZO–Ag nanorod LM (S = 598.5 nm per RIU) is remarkably greater than that of the GZO–Ag nanosphere (S = 428.2 nm per RIU) in the BW II while the S of the GZO–Ag nanorod TM (S = 267.14 nm per RIU) is smaller than that of the GZO–Ag spherical nanoshell (S = 314.21 nm per RIU) in BW I. In BW II, the FOM of the GZO–Ag nanorod LM is, on average, 1.5 times higher than that of the GZO–Ag spherical nanoshell over the entire range of n_{med}, and vice versa in the BW I.

In Fig. 8, we plot the resonance wavelength λ_{res} (on the left axis) and FOM factor (on the right axis) of the plasmon modes of the GZO–Ag nanorod and nanodisk *versus* the aspect ratio R of these structures at different values of the medium refractive
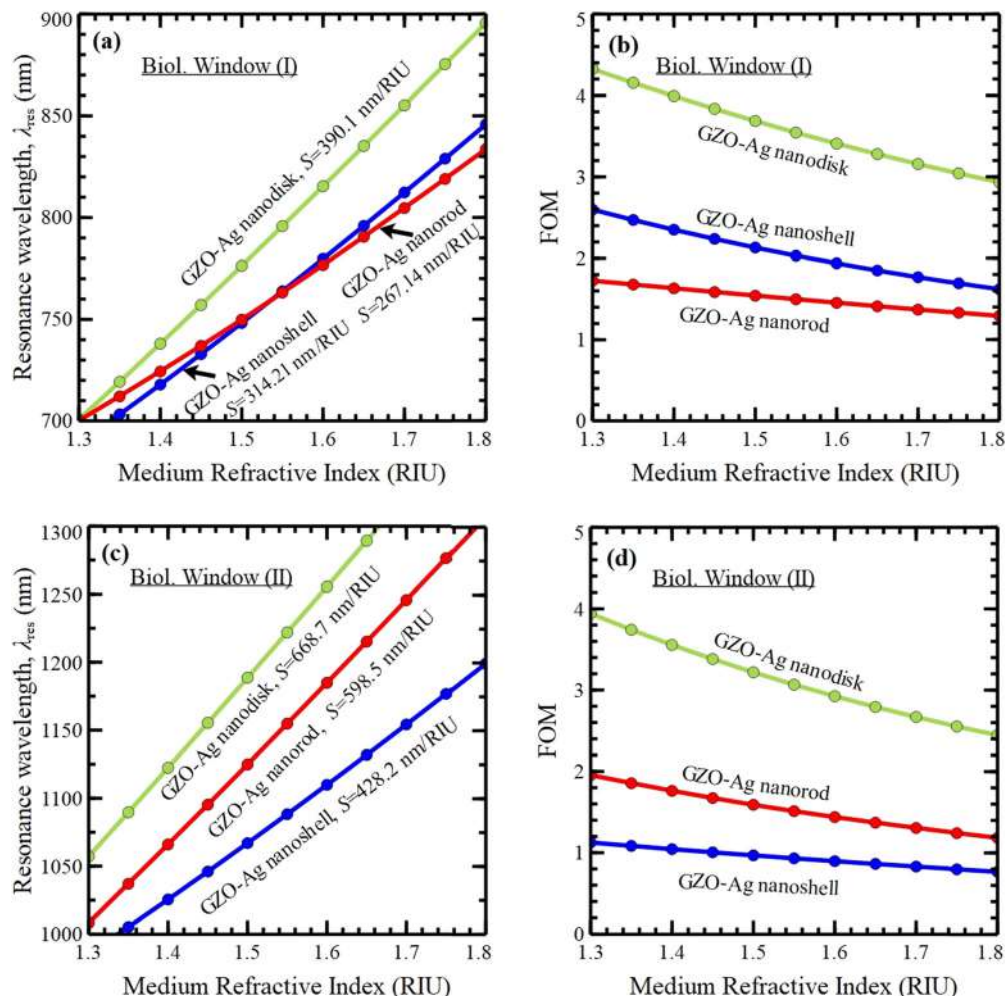
17826 | *Phys. Chem. Chem. Phys.*, 2024, **26**, 17817–17829

This journal is © the Owner Societies 2024

Fig. 7 Comparisons between the sensitivity S and FOM factors of the GZO−Ag spherical nanoshell, GZO−Ag nanorod, and GZO−Ag nanodisk, taking into consideration the spectral wavelength ranges of BW I in (a) and (b), and BW II in (c) and (d). The range of the medium's refractive index n_{med} for biological tissues ($\sim$1.3–1.8) is considered.

index n_{med}. Three values of n_{med} are taken, n_{med} = 1.33, 1.4, and 1.5. In Fig. 8, we take into account the second peak in the optical response spectra of the nanorod structure (LM peak) and nanodisk structure (TM peak) operated at longer wavelengths
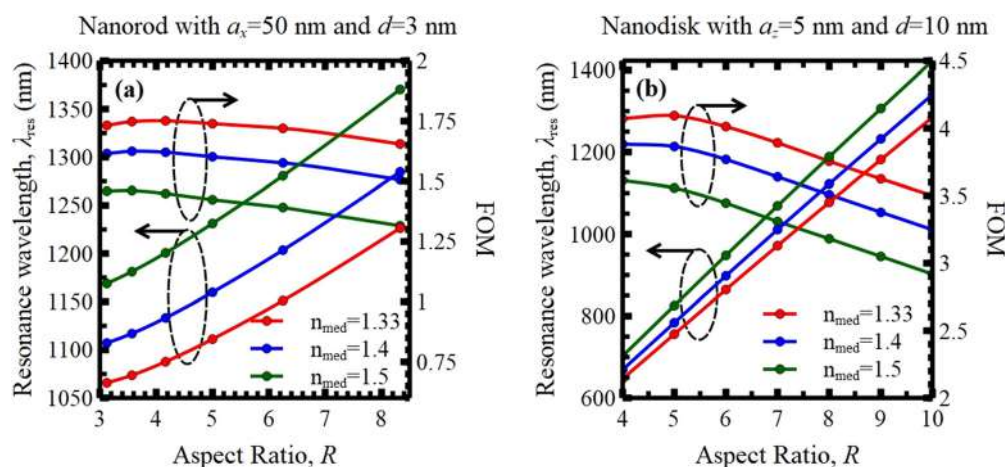

Fig. 8 The resonance wavelength λ_{res} (on the left axis) and FOM factor (on the right axis) of a plasmon mode *versus* the aspect ratio R at different values of the medium refractive index n_{med} for (a) GZO−Ag nanorod and (b) GZO−Ag nanodisk.

This journal is © the Owner Societies 2024

Phys. Chem. Chem. Phys., 2024, **26**, 17817–17829 | **17827**

(see Fig. (5)). For the GZO–Ag nanorod and nanodisk structures, the longitudinal length is held constant as shown in Fig. 7. The Ag shell thickness of the GZO–Ag nanorod and nanodisk d is assumed to be 3 nm and 10 nm, respectively. Then, the aspect ratio R is varied by changing the radial length r_1 in both structures. Comparing Fig. 8(a) with Fig. 8(b), it can be seen that the tunability of the GZO–Ag nanodisk with changing R is significantly higher than that of the GZO–Ag nanorod for the same range of R and n_{med}. For instance, for nanorod- and nanodisk-shaped nanoshells when $n_{med} = 1.33$, λ_{res} varies from 1075 nm to 1200 nm and varies from 650 nm to 1100 nm in the range of $R = 4–8$, respectively. It is worth noting that the latter observation does not depend on the Ag shell thickness d. As shown in Fig. 8(a) and (b), as R increases, the plasmon resonance peak red shifts almost linearly toward longer wavelengths associated with larger FWHM, and thus lower FOM. Overall, the FOM factor of both structures increases with increasing the shell thickness. However, considering the same shell thickness in both structures, the GZO–Ag nanodisk achieves a better FOM than that of the GZO–Ag nanorod.

4. Conclusion

We demonstrate that the plasmon resonances of nanoshell structures consisting of a GZO core surrounded by an Ag shell exhibit potential features for biosensing and biomedical applications in NIR BW I and II. We examine three distinct nanoshell shapes: the core–shell nanosphere (spherical nanoshell), nanorod, and nanodisk. In the case of the GZO–Ag nanorod and nanodisk, an effective medium approach is applied to calculate the dielectric function of a nanoshell structure as that of an equivalent homogenous spheroidal particle with an effective dielectric function. Then, the optical response of the spheroidal particle is calculated using the MLWA, which corrects the polarizability of the equivalent nanorod/nanodisk obtained using Gans theory. The validity of our approach is confirmed by means of comparisons with previously published numerical and experimental results. The MLWA-based method along with the exact Mie theory are used to calculate the optical response of GZO–Ag nanospheres. It is shown that by varying the geometrical parameters of the studied nanoshells, the plasmon resonances exhibit remarkable resonance tunability in the NIR range. The improved spectral characteristics and tunability of the plasmon resonances of GZO–Ag nanospheres make them a more promising platform for NIR applications than spherical metal colloids. Then, we show that core–shell nanorods and nanodisks, rather than GZO–Ag nanospheres, could significantly boost the sensitivity and FOM of the plasmon resonances. In terms of sensitivity and FOM, the transverse resonance optical properties of GZO–Ag nanodisks are superior to those of all plasmon resonances induced by the GZO–Ag nanorod and GZO–Ag nanosphere. In the BW I and BW II, the FOM of the GZO–Ag nanodisk transverse plasmon mode is nearly two orders of magnitude more than that of GZO–Ag nanorod's longitudinal and transverse plasmon modes. Also,

the transverse plasmon mode of the GZO–Ag nanodisk has a FOM that is 1.5 and 2 times greater than that of the plasmon mode of the GZO–Ag nanosphere.

Data availability

The data that support the findings of this study are available from the corresponding author upon reasonable request.

Author contributions

S. Moustafa: conceptualization, investigation, methodology, data curation, validation, formal analysis, writing – original draft preparation, writing – review and editing. J. Q. M. Almarashi: methodology, data curation, validation, formal analysis, writing – review and editing. M. K. Zayed: conceptualization, investigation, methodology, data curation, validation, formal analysis, writing – original draft preparation, writing – review and editing. M. Almokhtar: methodology, data curation, validation, formal analysis. M. Rashad: methodology, data curation, validation, formal analysis. H. Fares: conceptualization, investigation, methodology, data curation, validation, formal analysis, writing – original draft preparation, writing – review and editing.

Conflicts of interest

The authors declare no competing financial interest.

References

1 M. V. Kovalenko, L. Manna, A. Cabot, Z. Hens, D. V. Talapin, C. R. Kagan, V. I. Klimov, A. L. Rogach, P. Reiss and D. J. Milliron, *et al.*, *ACS Nano*, 2015, **9**, 1012–1057.

2 Y. Wang, H. Pei, Y. Jia, J. Liu, Z. Li, K. Ai, Z. Lu and L. Lu, *J. Am. Chem. Soc.*, 2017, **139**, 11616–11621.

3 C. von Roemeling, W. Jiang, C. K. Chan, I. L. Weissman and B. Y. S. Kim, *Trends Biotechnol.*, 2017, **35**, 159–171.

4 N. Cennamo, G. D'Agostino, C. Perri, F. Arcadio, G. Chiaretti, E. M. Parisio, G. Camarlinghi, C. Vettori, F. Di Marzo, R. Cennamo, G. Porto and L. Zeni, *Sensors*, 2021, **21**, 1681–1697.

5 C. Yu and J. Irudayaraj, *Anal. Chem.*, 2007, **79**, 572–580.

6 M. E. Stewart, C. R. Anderton, L. B. Thompson, J. Maria, S. K. Gray, J. A. Rogers and R. G. Nuzzo, *Chem. Rev.*, 2008, **108**, 494–521.

7 P. Singh, LSPR Biosensing: Recent Advances and Approaches, in *Reviews in Plasmonics*, ed. Geddes, C., Springer, Cham, 2016.

8 K. Liu, X. Xue and E. Furlani, *Sci. Rep.*, 2016, **6**, 34189–34196.

17828 | *Phys. Chem. Chem. Phys.*, 2024, **26**, 17817–17829

This journal is © the Owner Societies 2024

9 H. Nishi, K. Asami and T. Tatsuma, *Opt. Mater. Express*, 2016, **6**, 1043–1048.

10 C. Song, F. Li, X. Guo, W. Chen, C. Dong, J. Zhang, J. Zhang and L. Wang, *J. Mater. Chem. B*, 2019, **7**, 2001–2008.

11 A. J. Haes and R. P. Van Duyne, *J. Am. Chem. Soc.*, 2002, **124**, 10596–10604.

12 K.-S. Lee and M. A. El-Sayed, *J. Phys. Chem. B*, 2006, **110**, 19220–19225.

13 J. S. Sekhon and S. S. Verma, *J. Mater. Sci.*, 2012, **47**, 1930–1937.

14 I. Zorić, M. Zäch, B. Kasemo and C. Langhammer, *ACS Nano*, 2011, **5**, 2535–2546.

15 G. K. Joshi, S. Deitz-McElyea, M. Johnson, S. Mali, M. Korc and R. Sardar, *Nano Lett.*, 2014, **14**, 6955–6963.

16 F. Tam, C. Moran and N. Halas, *J. Phys. Chem. B*, 2004, **108**, 17290–17294.

17 H. Fares, M. Ahmed and S. Moustafa, *Phys. Scr.*, 2023, **98**, 035509–035522.

18 J. Q. M. Almarashi, S. Moustafa, M. Ahmed and H. Fares, *NANO*, 2023, **18**, 2350068–2350077.

19 H. Fares, M. Almokhtar, J. Q. M. Almarashi, M. Rashad and S. Moustafa, *Phys. E*, 2022, **142**, 115300–115309.

20 Y. Sun and Y. Xia, *Anal. Chem.*, 2002, **74**, 5297–5305.

21 M. Shabaninezhad and G. Ramakrishna, *J. Chem. Phys.*, 2019, **150**, 144116–144124.

22 Z.-W. Wu, Y.-W. Ma, Y.-Y. Jiang, J. Li, X.-C. Yin, L.-H. Zhang and M.-F. Yi, *Opt. Commun.*, 2019, **449**, 57–62.

23 A. Comin and L. Manna, *Chem. Soc. Rev.*, 2014, **43**, 3957–3975.

24 H. Y. Sohn and A. Murali, *Molecules*, 2021, **26**, 1456–1483.

25 S. D. Lounis, E. L. Runnerstrom, A. Llordés and D. J. Milliron, *J. Phys. Chem. Lett.*, 2014, **5**, 1564–1574.

26 O. Lupan, V. Cretu, V. Postica, M. Ahmadi, B. R. Cuenya, L. Chow, I. Tiginyanu, B. Viana, T. Pauporté and R. Adelung, *Sens. Actuators, B*, 2016, **223**, 893–903.

27 R. Chen, S. Luo, D. Xie, Y. Yu and L. Xiang, *Chemosensors*, 2022, **10**, 329–339.

28 A. Kołodziejczak-Radzimska and T. Jesionowski, *Materials*, 2014, **7**, 2833–2881.

29 C. Xu, L. Cao, G. Su, W. Liu, X. Qu and Y. Yu, *J. Alloys Compd.*, 2010, **497**, 373–376.

30 S.-J. Young, C.-C. Yang and L.-T. Lai, *J. Electrochem. Soc.*, 2017, **164**, B3013–B3028.

31 M. K. Hamza, J.-M. Bluet, K. Masenelli-Varlot, B. Canut, O. Boisron, P. Melinon and B. Masenelli, *Nanoscale*, 2015, **7**, 12030–12037.

32 T. B. H. Huynh, T. T. H. Nguyen, T. T. Tran, V. A. Duong, T. H. Pham and D. C. Nguyen, *J. Electron. Mater.*, 2020, **49**, 3964–3971.

33 U. K. Chettiar and N. Engheta, *Opt. Express*, 2012, **20**, 22976–22986.

34 A. Swaroop, A. Pujari and T. Thomas, *Materialia*, 2021, **19**, 101183–101191.

35 A. Kuzma, M. Weis, S. Flickyngerova, J. Jakabovic, A. Satka, E. Dobrocka, J. Chlpik, J. Cirak, M. Donoval, P. Telek, F. Uherek and D. Donoval, *J. Appl. Phys.*, 2012, **112**, 103531–103536.

36 *Absorption and Scattering of Light by Small Particles*, ed. C. F. Bohren and D. R. Huffman, Wiley-VCH Verlag GmbH, Weinheim, Germany, 1998.

37 K. M. Mayer and J. H. Hafner, *Chem. Rev.*, 2011, **111**, 3828–3857.

38 K. L. Kelly, E. Coronado, L. L. Zhao and G. C. Schatz, *J. Phys. Chem. B*, 2003, **107**, 668–677.

39 D. A. V. Bout, *J. Am. Chem. Soc.*, 2002, **124**, 7874–7875.

40 C. Langhammer, Z. Yuan, I. Zorić and B. Kasemo, *Nano Lett.*, 2006, **6**, 833–838.

41 E. J. Zeman and G. C. Schatz, *J. Phys. Chem.*, 1987, **91**, 634–643.

42 J. Zhao, A. O. Pinchuk, J. M. McMahon, S. Li, L. K. Ausman, A. L. Atkinson and G. C. Schatz, *Acc. Chem. Res.*, 2008, **41**, 1710–1720.

43 M. Locarno and D. Brinks, *Am. J. Phys.*, 2023, **91**, 538–546.

44 D. Schebarchov, B. Auguiéa and E. C. Le Ru, *Phys. Chem. Chem. Phys.*, 2013, **15**, 4233–4242.

45 G. Naik, J. Kim, N. Kinsey and A. Boltasseva, *Alternative Plasmonic Materials*, Handbook of Surface Science, North-Holland, 2014, ch. 6, vol. 4, pp. 189–221.

46 J. Kim, G. V. Naik, N. K. Emani, U. Guler and A. Boltasseva, *IEEE J. Sel. Top. Quantum Electron.*, 2013, **19**, 4601907–4601913.

47 G. V. Naik, V. M. Shalaev and A. Boltasseva, *Adv. Mater.*, 2013, **25**, 3264–3294.

48 H. Hövel, S. Fritz, A. Hilger, U. Kreibig and M. Vollmer, *Phys. Rev. B: Condens. Matter Mater. Phys.*, 1993, **48**, 18178–18188.

49 C. Jing, J. Shi and W. Tang, *J. Mater. Sci.*, 2019, **54**, 12659–12667.

50 J. Romann, J. Wei and M.-P. Pileni, *J. Phys. Chem. C*, 2015, **119**, 11094–11099.

51 A. D. Rakić, A. B. Djurišić, J. M. Elazar and M. L. Majewski, *Appl. Opt.*, 1998, **37**, 5271–5283.

52 Y. Gutierrez, D. Ortiz, R. A. de la Osa, J. M. Sanz, J. M. Saiz, F. Gonzalez and F. Moreno, *arXiv*, 2017, preprint, arXiv:1705.02248, DOI: **10.48550/arXiv.1705.02248**.

53 O. B. Toon and T. P. Ackerman, *Appl. Opt.*, 1981, **20**, 3657–3660.

54 N. Hooshmand, P. K. Jain and M. A. El-Sayed, *J. Phys. Chem. Lett.*, 2011, **2**, 374–378.

55 B. T. Draine and P. J. Flatau, *J. Opt. Soc. Am. A*, 1994, **11**, 1491–1499.

56 J. Mohanta, S. Satapathy and S. Si, *ChemPhysChem*, 2016, **17**, 364–368.

57 H. Baida, P. Billaud, S. Marhaba, D. Christofilos, E. Cottancin, A. Crut, J. Lermé, P. Maioli, M. Pellarin, M. Broyer, N. Del Fatti, F. Vallee, A. Sánchez-Iglesias, I. Pastoriza-Santos and L. M. Liz-Marzán, *Nano Lett.*, 2009, **9**, 3463–3469.

58 S. Moustafa, M. K. Zayed, M. Ahmed and H. Fares, *Phys. Chem. Chem. Phys.*, 2024, **26**, 1994–2006.

59 S. A. Lee and S. Link, *Acc. Chem. Res.*, 2021, **54**, 1950–1960.

60 Y. M. Lee, S. E. Kim and J. E. Park, *Nano Convergence*, 2023, **10**, 34–61.

61 S. Link and M. A. El-Sayed, *J. Phys. Chem. B*, 1999, **103**, 8410–8426.

62 L. Hirsch, A. Lowery, R. Drezek, N. Halas and J. West, *Ann. Biomed. Eng.*, 2006, **34**, 15–22.

63 C. Z. Tan, *J. Non-Cryst. Solids*, 1998, **223**, 158–163.

64 J. R. Devore, *J. Opt. Soc. Am.*, 1951, **41**, 416–419.

65 R. Khan, B. Gul, S. Khan, H. Nisar and I. Ahmad, *Photodiagn. Photodyn. Ther.*, 2021, **33**, 10192–10200.

This journal is © the Owner Societies 2024

Phys. Chem. Chem. Phys., 2024, **26**, 17817–17829 | **17829**